

# Nonlinear Topological Edge States: from Dynamic Delocalization to Thermalization

Bertin Many Manda,<sup>1,2</sup> Rajesh Chaunsali,<sup>1,3</sup> Georgios Theocharis,<sup>1</sup> and Charalampos Skokos<sup>2</sup>

<sup>1</sup>LAUM, CNRS, Le Mans Université, Avenue Olivier Messiaen, 72085 Le Mans, France

<sup>2</sup>Nonlinear Dynamics and Chaos group, Department of Mathematics and Applied Mathematics, University of Cape Town, Rondebosch, 7701 Cape Town, South Africa

<sup>3</sup>Department of Aerospace Engineering, Indian Institute of Science, Bangalore 560012, India

(Dated: December 28, 2021)

We consider a mechanical lattice inspired by the Su–Schrieffer–Heeger model along with cubic Klein-Gordon type nonlinearity. We investigate the long-time dynamics of the nonlinear edge states, which are obtained by nonlinear continuation of topological edge states of the linearized model. Linearly unstable edge states delocalize and lead to chaos and thermalization of the lattice. Linearly stable edge states also reach the same fate, but after a critical strength of perturbation is added to the initial edge state. We show that the thermalized lattice in all these cases shows an effective renormalization of the dispersion relation. Intriguingly, this renormalized dispersion relation displays a unique symmetry, i.e., its square is symmetric about a finite squared frequency, akin to the chiral symmetry of the linearized model.

## I. INTRODUCTION

The problem of energy transport and ensuing *thermalization in nonlinear discrete lattices* has attracted a lot of attention over the past decades, starting with the acclaimed numerical experiment of Fermi, Pasta, Ulam and Tsingou [1–4] to its far reaching implications in understanding integrable and non-integrable dynamical systems with applications to statistical mechanics, ergodicity and chaos (see e.g., [5–10]). One central and long-standing question is whether and how the intrinsic dynamics of a discrete nonlinear lattice leads to chaos, thermalization and energy equipartition across all the normal modes (NMs). Several works have addressed this question for many different one-dimensional (1D) lattice models. In [11], dynamical regimes in the parameter space of the discrete nonlinear Schrödinger (DNLS) system leading to thermalization or to the appearance of localized motions were identified, while energy thresholds allowing the emergence of such localized structures were obtained in [12]. Furthermore, the chaotic dynamics of the model was investigated in more detail in [13] by means of the Lyapunov exponents spectrum. Studies of the disordered version of the DNLS system, where all linear modes are exponentially localized, showed that the nonlinear dynamics leads to energy delocalization [14], chaos [15] and thermalization [16]. The onset of thermalization and equipartition due to the nonlinear interactions between normal modes for the discrete nonlinear Klein-Gordon (KG) lattice was studied in [17], while the chaotic spreading of initially localized excitations in the disordered KG system was investigated in [15, 18].

In recent years, *topological discrete lattices* have attracted a sheer amount of attention in theory and experiments [19–21]. The core concept involves designing systems with nontrivial band topology that results in boundary states robust to lattice’s imperfection and/or smooth deformation. While these so-called topological states are well defined in the linear limit, there has been an intense and increasing interest, mostly in the fields of photon-

ics, electronics (see for example [22]) and mechanics [23–30], to what happens when nonlinear effects enter into play. Depending on the functional form of the nonlinearity, the latter can modify the shape, the frequency and more importantly the stability of the topological edge modes [31–34]. The presence of nonlinearity, can also lead to the formation of topologically-robust edge solitons [35], unique gap solitons [36], or “self-induced” edge solitons and domain walls [25, 37, 38]. Finally, nonlinear, periodically driven topological lattices have been also investigated both theoretically and experimentally [35, 39–43].

All these works contribute to our understanding of how topological states behave or emerge in the presence of inter-particle interactions and nonlinearity. However, very little is known about the long time behavior of these nonlinear topological states [44]. Even, when a linear stability analysis is performed [32, 34], this is able only to describe the short time dynamics. Since, the nonlinearity in general breaks the integrability of the underlined discrete lattice dynamical system, equipartition or energy localization are the only two possibilities for long times.

Topological lattices possess robust edge states within a topologically protected band gap. Since this scenario is absent in generic nonlinear lattice models (see, e.g. [1–3]) a series of questions with a fundamental theoretical interest arise. Do topological, nonlinear discrete lattices, reach thermalization? Can nonlinear topological edge states use as initial conditions on a topological lattice, remain localized under the presence of perturbations, or a dynamical delocalization is expected? Considering that the nonlinear topological lattice has reached thermalization, can one, along the lines of [45, 46], describe the system by an *effective* dispersion relation with some unique symmetry properties inherited from the dispersion relation of the linearized topological lattice?

Trying to answer these questions, we perform here a follow up systematic analysis of the long time dynamics of nonlinear edge states, that were analyzed in a mechanical lattice with KG-type nonlinearity [32]. In the linearized

limit, this model is inspired from the well-celebrated Su–Schrieffer–Heeger (SSH) lattice [47], in which topological protection of the edge states stems from chiral symmetry of the Hamiltonian [48]. However, their difference lies in the fact that the band gap falls in finite (non-zero) frequency range in the former [32], and hence, the edge states have vibratory nature. It was shown in [32] that nonlinear continuations of topological edge states could pass through regions of linear stability and instability depending on the sign and the strength of the nonlinearity.

Here, we investigate the *long-time* chaotic dynamics of *unstable* states to be able to answer the question if the system achieves equipartition in a long time. Moreover, we investigate if the linearly *stable* edge states can also be delocalized due to strong perturbations, and eventually, lead to equipartition. We demonstrate that despite the presence of the band gap into the frequency spectrum, which may prevent part of the energy of the edge state to propagate away from the edges, *linearly unstable*, topological nonlinear edge states seen in Ref. [32], lead to thermalization of the lattice well described by a Gibbs distribution. Then, focusing on the *linearly stable* topological nonlinear edge states seen in Ref. [32], we discuss the condition under which these lose their stability and lead to thermalization too. In both cases, by calculating the renormalized dispersion relation for the thermalized state, we find, remarkably, that this possesses a unique symmetry akin to chiral symmetry seen in the dispersion of the linearized lattice.

The paper is organized as follows. In Sec. II we introduce the Hamiltonian formalism of the model in our study. In Sec. III, we present the method for obtaining linear edge states and their nonlinear continuations, discussing their spatial and spectral properties. In Sec. IV, we present the computational foundations of our numerical investigation. Section V contains our numerical results, which are mainly focused on the energy spreading of unstable topological nonlinear edge states, renormalized dispersion of the thermalized state, as well as the robustness of stable edge states to increasing perturbations. Finally in Sec. VI we conclude our work and present some open avenues for future research.

## II. MODEL DESCRIPTION

Our system is a lattice of  $n$  coupled identical particles (see Fig. 1). These particles are interconnected with alternating binary springs of strengths  $1 - \gamma$  and  $1 + \gamma$ , and are subject to onsite nonlinear potentials whose elastic and nonlinear coefficient values are given by  $\gamma_0$  and  $\Gamma$  respectively [32]. In the limit  $\gamma \rightarrow 0$  we recover the monomer KG chain [17, 49]. As an additional remark, we note that when  $\Gamma < 0$  the system possesses escape energy thresholds. The total energy of a lattice is given

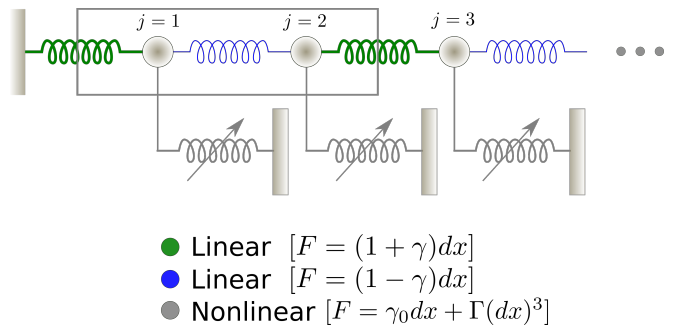


Figure 1. A semi-infinite chain consisting of equal masses [grey spheres] interconnected with two types of linear springs with elastic constants  $1 + \gamma$  and  $1 - \gamma$ , denoted by the green and blue spiral coils respectively. Each mass is grounded with a nonlinear spring [grey spiral coil] whose elastic and nonlinear constants are  $\gamma_0$  and  $\Gamma$ . The  $dx$  denotes the spring deformation and  $F$  the resulting external force applying to a single mass.

by the Hamiltonian function

$$\begin{aligned} \mathcal{H} &= \mathcal{H}_2 + \mathcal{H}_4, \quad \mathcal{H}_4 = \frac{\Gamma}{4} \sum_{j=1}^n x_j^4, \\ \mathcal{H}_2 &= \frac{1}{2} \sum_{j=1}^n [p_j^2 + \gamma_0 x_j^2] \\ &+ \frac{1}{4} \sum_{\substack{j=1 \\ j=\text{odd}}}^n \left[ (1 + \gamma) (x_j - x_{j-1})^2 + (1 - \gamma) (x_{j+1} - x_j)^2 \right] \\ &+ \frac{1}{4} \sum_{\substack{j=0 \\ j=\text{even}}}^n \left[ (1 - \gamma) (x_j - x_{j-1})^2 + (1 + \gamma) (x_{j+1} - x_j)^2 \right], \end{aligned} \quad (1)$$

where,  $x_j$  and  $p_j$  are the displacements from the equilibrium points, and the associated momentum of the  $j$ th particle. It should be emphasized that the quartic term  $\mathcal{H}_4$  is of KG type nonlinearity. Further, as we are going to see in Sec. III, under proper boundary conditions, the Hamiltonian model [Eq. (1)] allows for (non)linear topological edge states.

The lattice's equations of motion are derived from the Hamiltonian function  $\mathcal{H}$  [Eq. (1)] taking into account that the pair  $x_j, p_j$  are canonical conjugate variables

$$\begin{aligned} \dot{x}_j &= p_j, \\ \dot{p}_j &= -(1 + \gamma) (x_j - x_{j-1}) + (1 - \gamma) (x_{j+1} - x_j) \\ &\quad - \gamma_0 x_j - \Gamma x_j^3 \quad \text{if } j \text{ odd}, \\ \dot{p}_j &= -(1 - \gamma) (x_j - x_{j-1}) + (1 + \gamma) (x_{j+1} - x_j) \\ &\quad - \gamma_0 x_j - \Gamma x_j^3 \quad \text{if } j \text{ even}, \end{aligned} \quad (2)$$

with  $(\dot{\phantom{x}})$  denoting the time derivative. The full set of equations [Eq. (2)] conserves the value of the Hamiltonian function [Eq. (1)] which could therefore be used as our

control parameter of the nonlinearity strength when  $\gamma_0$ ,  $\gamma$  and  $\Gamma$  remain fixed.

A common way to investigate the system's thermalization is through the dynamics of its NMs [16, 49–51]. The NM coordinate is defined by [45, 46, 52]

$$a_k = \frac{1}{\sqrt{2\omega_k(\gamma)}} [P_k + i\omega_k(\gamma) Q_k], \quad (3)$$

where  $Q_k$ ,  $P_k$  are the discrete Fourier transform of the canonical coordinates  $x_j$  and momenta  $p_j$ , and  $\omega_k(\gamma)$  is the frequency of mode  $k$ . For the case of periodic boundary conditions, the two bands of the dispersion relation are given by:

$$\omega_k = \left( 2 + \gamma_0 \pm \sqrt{2(1 + \gamma^2) + 2(1 - \gamma^2) \cos(2k\pi/n)} \right)^{1/2}. \quad (4)$$

Thus,  $\gamma$  adjusts the size of the band gap in the dispersion relation (see Sec. III). In the normal variables, the Hamiltonian function  $\mathcal{H}$  [Eq. (1)] is written as

$$\begin{aligned} \mathcal{H} &= \hat{\mathcal{H}}_2 + \hat{\mathcal{H}}_4, \quad \hat{\mathcal{H}}_2 = \sum_{k=0}^n \omega_k(\gamma) |a_k|^2, \\ \hat{\mathcal{H}}_4 &= \Gamma V(a_1, a_2, \dots, a_n), \end{aligned} \quad (5)$$

where  $V(a_1, a_2, \dots, a_n)$  is a linear combination of quartic products of  $a_k$  and  $a_k^*$  [17, 51]. Consequently the equations of motion become  $i\dot{a}_k = \partial\mathcal{H}/\partial a_k^*$ . Here the  $(^*)$  denotes the complex conjugate.

### III. TOPOLOGICAL (NON-)LINEAR EDGE STATES

Since our system is the one studied in Ref. [32], in this section we provide a very brief review of essential details on the characteristics of topological states to be useful in the current study. We can get the first insight on the nature of our system by evaluating its dispersion properties in the linear limit ( $\Gamma = 0$ ) through the solution of an eigenvalue problem of a dynamical matrix. This matrix is akin to the Hamiltonian of the SSH model [47] apart from the fact that its diagonal elements are nonzero. Consequently, the eigenvalues ( $\omega^2$ ), are symmetric about the mid gap frequency  $\omega^2 = 2 + \gamma_0$  due to chiral symmetry of the dynamical matrix [48]. The symmetry makes it possible to characterize the dynamical matrix with a topological invariant, e.g., winding number. The system can be shown to make a topological transition when the parameter  $\gamma$  varies from negative to positive values, or in other words, band gap closes and opens again [48].

According to the bulk-boundary correspondence, the topological transition of the *infinite* lattice as discussed above reflects as the emergence of edge states in the *finite* chain [19]. For all the cases in this work, we take a long chain of  $n = 100$  particles, to avoid strong finite size effects. We also consider fixed (free) boundary condition

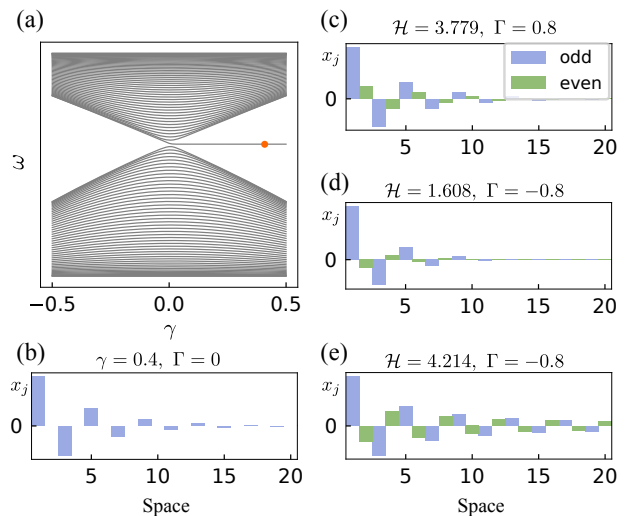


Figure 2. Nonlinearity-modified topological edge states. (a) Emergence of topological edge state inside the band gap. (b) Spatial profile,  $x_j$  of the edge state with  $\gamma_0 = 1$  and  $\gamma = 0.4$  whose frequency is indicated by the red dot in panel (a). (c)–(e) Nonlinear continuations of the topological edge state for ( $\mathcal{H} = 3.779, \Gamma = 0.8$ ), ( $\mathcal{H} = 1.608, \Gamma = -0.8$ ) and ( $\mathcal{H} = 4.214, \Gamma = -0.8$ ), respectively. In all the cases, the chosen profile of the mode is such that the corresponding momentum profile is zero,  $p_j=0$ .

for the left (right) end of the chain. This choice ensures the existence of only one edge state localized around the fixed boundary. We note that in the case of even number of particles and with fixed boundary conditions in both ends, two hybridized edge states are expected, see for example [53]. In Fig. 2(a), we show the spectrum of this finite chain when  $\gamma_0 = 1$ . Due to the topological transition at  $\gamma = 0$ , we observe the emergence of a state pinned at  $\omega^2 = 2 + \gamma_0$  inside the band gap for  $\gamma > 0$ . This state is exponentially localized on the left edge, as shown in Fig. 2(b) for  $\gamma = 0.4$ . Moreover, the state has zero amplitude at even sites as a result of chiral symmetry. Such a state is of topological origin and protected by chiral symmetry.

Once nonlinearity is turned on, i.e.,  $\Gamma \neq 0$  in  $\mathcal{H}$  [Eq. (1)], we calculate the time-periodic solutions using Newton's method in the system's phase space (see e.g. [54]) with the aforementioned edge state as the initial condition. Moreover, we determine the linear stability of such nonlinear states using Floquet theory [55]. In Ref. [32] it was shown that the topological edge state changes its frequency, shape, and stability depending on the sign of nonlinearity and increasing its energy, thus the strength of nonlinearity. We show a few representative cases in Figs. 2(c)–(e). These are not only distinct from the linear edge state shown in Fig. 2(b) in that they no longer retain the chiral profile with vanishing amplitudes at even sites, but also they have different instabilities. For example, the stiffening ( $\Gamma > 0$ ) case shown in Fig. 2(c) with ( $\mathcal{H} = 3.779, \Gamma = 0.8$ ) is a linearly stable

solution. Whereas the softening ( $\Gamma < 0$ ) cases shown in Figs. 2(d) and 2(e) with ( $\mathcal{H} = 1.608, \Gamma = -0.8$ ) and ( $\mathcal{H} = 4.214, \Gamma = -0.8$ ), respectively, are unstable solutions.

## IV. COMPUTATIONAL FRAMEWORK

### A. Equipartition

In order to clarify the thermal properties of our topological lattice, we follow the observables of the system in the NM and real phase spaces. In the Fourier (NM) space, we follow the time evolution of the normalized modal energy [50]

$$\nu_k(t) = \frac{E_k(t)}{\hat{\mathcal{H}}_2(t)}, \quad E_k(t) = \omega_k(\gamma) |a_k(t)|^2, \quad (6)$$

where  $\hat{\mathcal{H}}_2(t) = \sum_k E_k(t)$  is the total quadratic energy of the modes of Eq. (5) and  $E_k$  the energy of the  $k$ th mode. We characterize the degree of spreading of  $\nu_k$  in Eq. (6) using the spectral entropy [56–59]

$$S(t) = - \sum_k \nu_k(t) \ln[\nu_k(t)], \quad 0 \leq S(t) \leq \ln n. \quad (7)$$

If the total energy  $\hat{\mathcal{H}}_2$  [Eq. (5)] is localized on a single mode,  $S = 0$ . On the other hand, if the energy  $\hat{\mathcal{H}}_2$  is uniformly distributed across all modes,  $S = \ln n$ . In order to mitigate the dependence on the lattice size  $n$  of  $S$  [Eq. (7)], it is more convenient to use the rescaled spectral entropy [56–59]

$$\eta(t) = \frac{S(t) - S_{max}}{S(0) - S_{max}}, \quad 0 \leq \eta(t) \leq 1, \quad (8)$$

with  $S_{max} = \ln n$ . In this way, when the whole energy is concentrated at one mode  $\eta = 1$ , while  $\eta = 0$  corresponds to a uniform distribution of the energy throughout all the modes. If we consider that the modal energies at thermal equilibrium are characterized by a Gibbs distribution

$$\rho_{G,k} = \frac{1}{\mathcal{Z}} e^{-\beta E_k}, \quad \mathcal{Z} = \sum_k e^{-\beta E_k}, \quad (9)$$

where  $\rho_{G,k}$  corresponds to the probability to find a mode  $k$  with energy  $E_k$ ,  $\mathcal{Z}$  equals the partition function and  $\beta$  is the inverse temperature, we find that the value of  $\eta(t)$  [Eq. (8)] at thermal equilibrium fluctuates about the average [59]

$$\langle \eta \rangle_G = \frac{1 - C}{S_{max} - S(0)}, \quad (10)$$

where  $C \approx 0.5772$  is the Euler constant.

To account for the phase space dynamics, we compute the normalized energy per site

$$\xi_j(t) = \frac{h_j(t)}{\mathcal{H}}, \quad \mathcal{H} = \sum_j h_j(t), \quad (11)$$

where the energy at the  $j$ th site in the bulk is given by

$$\begin{aligned} h_j &= p_j^2/2 + \gamma_0 x_j^2/2 + \Gamma x_j^4/4 + (1 + \gamma)(x_j - x_{j-1})^2/4 \\ &\quad + (1 - \gamma)(x_{j+1} - x_j)^2/4 \quad \text{if } j \text{ odd,} \\ h_j &= p_j^2/2 + \gamma_0 x_j^2/2 + \Gamma x_j^4/4 + (1 - \gamma)(x_j - x_{j-1})^2/4 \\ &\quad + (1 + \gamma)(x_{j+1} - x_j)^2/4 \quad \text{if } j \text{ even.} \end{aligned} \quad (12)$$

For the edge sites respectively with indices  $j = 1$  and  $j = n$ , we have

$$\begin{aligned} h_1 &= p_1^2/2 + \gamma_0 x_1^2/2 + \Gamma x_1^4/4 + (1 + \gamma)x_1^2/4 \\ &\quad + (1 - \gamma)(x_2 - x_1)^2/4, \quad \text{and} \\ h_n &= p_n^2/2 + \gamma_0 x_n^2/2 + \Gamma x_n^4/4 + (1 + \gamma)(x_n - x_{n-1})^2/4, \end{aligned} \quad (13)$$

considering fixed boundary condition for the left ( $x_0 = 0$ ) and free boundary condition for the right ( $x_{n+1} = x_n$ ) end of the chain. Then, the degree of inhomogeneity of the spatial distribution of the energy is well characterized by the participation number

$$P^{-1}(t) = \sum_j \xi_j^2(t), \quad 1 \leq P(t) \leq n. \quad (14)$$

When the total energy  $\mathcal{H}$  is concentrated only on one excited site,  $P = 1$  while in case of equipartition of the energy among all sites,  $P = n$ .

### B. Chaotization

As an additional characterization of the lattice's equipartition state, we compute the finite-time maximum Lyapunov exponent (ftMLE) [60–63]

$$\lambda(t) = \frac{1}{t} \ln \left( \frac{\|\mathbf{W}(t)\|}{\|\mathbf{W}(0)\|} \right), \quad (15)$$

which quantifies the exponential growth rate at time  $t$  of the separation  $\mathbf{W}(t)$  in the phase space between two initially nearby orbits, so that  $\|\mathbf{W}(0)\| \rightarrow 0$ , with  $\|\cdot\|$  being the usual Euclidean norm. More specifically, the  $\mathbf{W}(0) = \delta\mathbf{X}(0) = (\delta x_1(0), \delta x_2(0), \dots, \delta x_n(0), \delta p_1(0), \dots, \delta p_n(0))$  can be viewed as a small perturbation to the system's initial position  $\mathbf{X}(0) = (x_1(0), x_2(0), \dots, x_n(0), p_1(0), \dots, p_n(0))$  in the phase space, whose time evolution is governed by equations (referred to as variational equations) derived from the linearization of the system's Hamilton equations of motion [64]. Consequently the maximal Lyapunov exponent (MLE) [61–63]

$$\Lambda = \lim_{t \rightarrow \infty} \lim_{\|\mathbf{W}(0)\| \rightarrow 0} \lambda(t), \quad (16)$$

measures the strength of chaos in the system.

In thermal equilibrium, all the modes are heated and randomly interact in order to spatially homogenize chaos inside the lattice [15, 18, 65, 66]. Therefore equipartition is associated to a constant positive ftMLE [2, 58, 60, 65, 67].



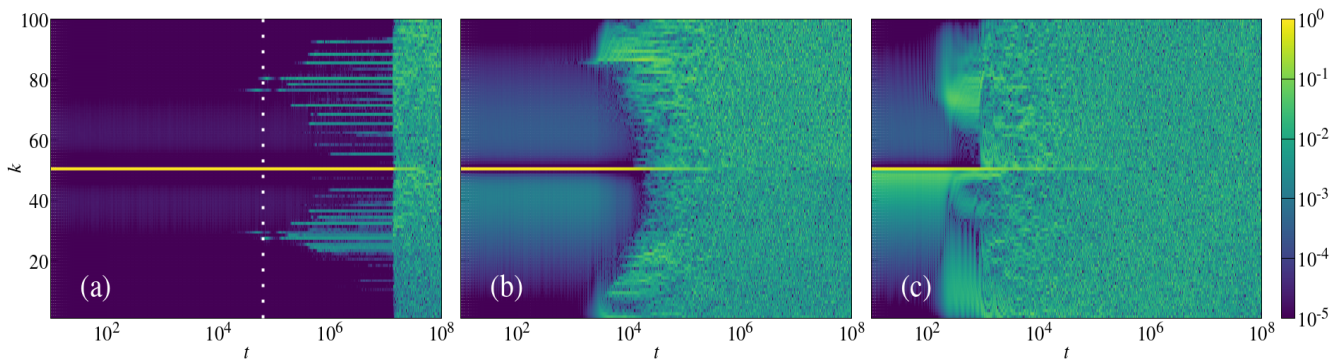


Figure 3. The normalized modal energy  $\nu_k(t)$  [Eq. (6)] evolution profiles for representative realizations of setup [Eq. (17)] of three different nonlinear topological edge states at  $(\mathcal{H}, \Gamma)$  values with  $(\mathcal{H} = 0.307, \Gamma = -0.8)$ ,  $(\mathcal{H} = 1.608, \Gamma = -0.8)$  and  $(\mathcal{H} = 4.214, \Gamma = -0.8)$  in panels (a), (b) and (c) respectively. The white vertical line in (a) shows the position of the cross section of  $\nu_k(t)$  at  $t \approx 6.3 \times 10^4$  depicted in Fig. 11 of App. B. The edge states associated with panels (b) and (c) are respectively shown in Figs. 2(d) and (e). Each point is colored according to the color scale at the right end of the figure.

## V. NUMERICAL SIMULATIONS

In this section we present the numerical results obtained by evolving several perturbations of nonlinear topological localized states when both the energy and the sign of the onsite nonlinear strength are varied. The numerical integration of the equations of motion and the variational equations of the model [Eq. (1)] is done by the implementation of the `AB4864` symplectic scheme of order 4 (see App. A for details). The final integration time is  $T \approx 10^6 - 10^9$ , and we set the integration time step to  $\tau = 0.2$  so that the relative energy error,  $E_r(t) = |[\mathcal{H}(t) - \mathcal{H}(0)]/\mathcal{H}(0)|$ , remains below  $E_r = 10^{-5}$  for the duration of all our simulations.

For all the cases presented in this work, the lattice size is fixed at  $n = 100$  particles, and the elastic parameters kept to  $\gamma_0 = 1$  and  $\gamma = 0.4$ . The choice of these elastic parameters leads to a relatively large band gap, Fig. 2(a). Investigating the cases of different values of  $\gamma$ , which controls the width of the frequency gap, is an interesting problem which however, is out of the scope of this work. As we noted above, fixed and free boundary conditions are used for the left and right end of the chain, a choice which ensures the existence of only one edge state located around the left end of the chain.

Let us discuss now in some detail the initial conditions we use in our simulations. In the Fourier space representation, the topological edge state  $\mathbf{X}^b = (x_1^b, x_2^b, \dots, x_n^b, p_1^b, p_2^b, \dots, p_n^b)$  has coordinates  $(Q_1^b, Q_2^b, \dots, Q_n^b, P_1^b, P_2^b, \dots, P_n^b)$  such that in NM variables,  $\mathbf{X}^b = (a_1^b, a_2^b, \dots, a_n^b)$  with  $a_k^b = (P_k^b + i\omega_k(\gamma)Q_k^b)/\sqrt{2\omega_k(\gamma)}$  [Eq. (3)].  $\omega_k(\gamma)$  corresponds to the eigenfrequencies of the finite chain with the above mentioned boundary conditions and elastic parameters. We calculate these numerically by diagonalizing the system's dynamical matrix. We initially start with the topological localized state on which a real random phase  $\varepsilon_k$  is added

in its Fourier representation

$$a_k(t=0) = a_k^b e^{i\varepsilon_k}, \quad \text{if } 1 \leq k \leq n, \quad (17)$$

such that all the derived initial conditions possess the same linear energy as the edge state  $\mathbf{X}^b$ . Unless otherwise stated, we use a uniform probability distribution to set the perturbation parameters  $\varepsilon_k$  with values on the interval  $[-10^{-2}, 10^{-2}]$ .

In order to compute the ftMLE we choose the coordinates of the initial deviation vector  $\mathbf{W}(t=0)$  as randomly selected numbers drawn from a uniform distribution in the interval  $[-1, 1]$ . The non-zero coordinates of  $\mathbf{W}(0)$  are located only inside the localization volume [68] of the linear topological edge state [32] (see also Sec. III). It is worth mentioning that the final value of the long-time evolution of the ftMLE [Eq. (15)] used to estimate the MLE [Eq. (16)] does not practically depend on the choice of the initial deviation vector [63].

### A. Characteristics of unstable topological edge state delocalization

To provide a feeling of the thermalization of the lattice [Eq. (1)] starting from unstable nonlinear topological edge states, we consider the sets of parameters  $(\mathcal{H} = 0.307, \Gamma = -0.8)$ ,  $(\mathcal{H} = 1.608, \Gamma = -0.8)$  and  $(\mathcal{H} = 4.214, \Gamma = -0.8)$  of the setup [Eq. (17)]. The two latter correspond to the edge states shown in Figs. 2(d)–2(e). We set the perturbation parameters  $\varepsilon_k = \pm 10^{-2}$ . The amplitude profiles of the distribution of the normalized energy per mode  $\nu_k(t)$  [Eq. (6)] is shown for representative realizations in Fig. 3. For all values of  $\mathcal{H}$  [Eq. (1)], the delocalization of unstable nonlinear topological edge states leads to the thermalization of the lattice at finite time scales.

For example, in Fig. 3(a), the normalized energy profile of the case  $(\mathcal{H} = 0.307, \Gamma = -0.8)$  is shown. This

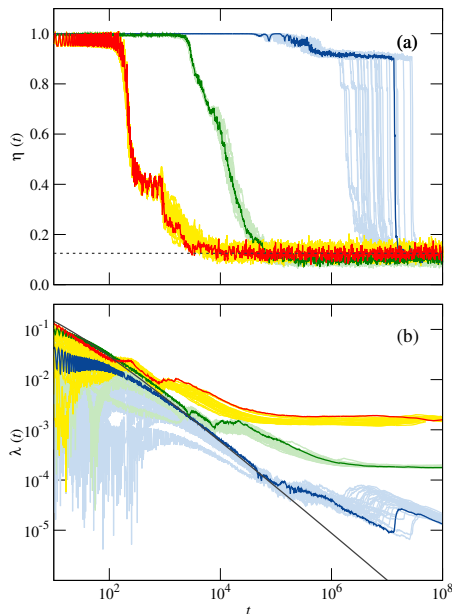


Figure 4. Temporal evolution of the (a) rescaled spectral entropy  $\eta(t)$  [Eq. (8)] and (b) the ftMLE  $\lambda(t)$  [Eq. (15)] of the model [Eq. (1)] for representative realizations of the initial nonlinear topological edge states with  $(\mathcal{H} = 0.307, \Gamma = -0.8)$  [blue],  $(\mathcal{H} = 1.608, \Gamma = -0.8)$  [green] and  $(\mathcal{H} = 4.214, \Gamma = -0.8)$  [red] of Fig. 3. The black dashed horizontal line in (a) measures  $\langle \eta \rangle_G \approx 0.125$ , the Gibbs average for the case  $(\mathcal{H} = 4.214, \Gamma = -0.8)$  [red curves in panels (a) and (b)]. The shaded curves around the dark-colored curves' course represent the evolution of 30 other realizations of perturbation of the same topological edge states. The black solid line in (b) shows the relation  $\lambda(t) \propto \ln(t)/t$  observed in the case of regular motion.

initial condition corresponds to a weakly unstable nonlinear edge state with “bulk-bulk” instability, which is caused by the collision of two *bulk* modes (both spatially extended) [32]. It is known [69] that these instabilities are caused by finite-size effects and that they are vanishing in the thermodynamic limit. After a transient period of the order of  $\approx 10^4$  time units, only 4 modes in the acoustic (2 modes) and optical (2 modes) bands initially resonate. We have checked that these initially excited modes of Fig. 3(a), correspond to the frequencies of the most unstable eigenvectors of the Floquet analysis [32], see App. B. Afterward, a cascading effect of resonances between NMs is taking place up to complete thermalization of the lattice at about  $10^7$  time units. We have also checked that by increasing the size of the lattice to 1000 particles, the instability and the resulting thermalization appears later, confirming the finite-size origin of this weak instability.

On the other hand, in Figs. 3(b,c), the normalized energy profile of the cases  $(\mathcal{H} = 1.608, \Gamma = -0.8)$  and  $(\mathcal{H} = 4.214, \Gamma = -0.8)$  are shown. These initial conditions correspond to strongly unstable nonlinear edge states with

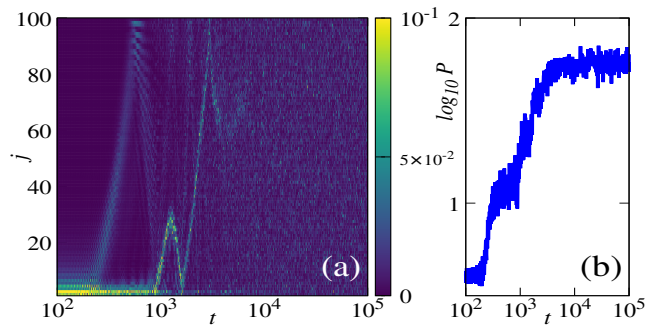


Figure 5. (a) Spatiotemporal profile of the normalized energy distribution  $\xi_j(t)$  [Eq. (11)] for the case  $(\mathcal{H} = 4.214, \Gamma = -0.8)$  of Figs. 3(c) and 4 (red curves in that figure). Each lattice site is colored according to the magnitude of its  $\xi_j$  value [see colorscale at the right of (a)]. (b) Evolution of the associated participation number  $P(t)$  [Eq. (14)]. We see that the saturation of the entropy  $\eta(t)$  [red curve in Fig. 4(a)] practically coincides with the one displayed by  $P(t)$  in panel (b).

“edge-bulk” instability, which is caused by the collision of one *bulk* mode (spatially extended) with an edge mode (localized) [32]. This kind of instability is present even in the thermodynamic limit. In contrast with the previous case of Fig. 3(a), one observes the excitation of almost continuous bands (in the optical and acoustic frequencies) of modes. The size of these excited bands, grows increasing the value of the energy [see Figs. 3(b) and (c)]. This efficient and broadband excitation may be related to the onset of the Chirikov criterion [70], which predicts an energy threshold above which effective (fast) energy transfer between NMs takes place [3, 46]. Since these energy transfers homogenize chaos within the lattice interior, we also expect the chaotic dynamics to be stronger [3, 65, 71], and the system to thermalize faster, as indeed it is observed in Figs. 3(b) and (c).

The thermalization and chaotization of system [Eq. (1)] are further confirmed from the computation of the rescaled entropy  $\eta(t)$  [Eq. (8)], of the normalized energy per mode, and the ftMLE,  $\lambda(t)$  [Eq. (15)] (Fig. 4). In Fig. 4(a), the rescaled spectral entropy  $\eta$  [Eq. (8)] is plotted as a function of time  $t$ , for the three sets of parameters used in Fig. 3. All curves start at  $\eta = 1$ , at time  $t = 0$  and then decline to settle toward values well approximated by the (Gibbs) ensemble average  $\langle \eta \rangle_G$  [Eq. (10)] with values  $\approx 0.092, 0.096$  and  $0.125$  [black dashed line in Fig. 4(a)] for the cases with  $\mathcal{H} = 0.307, 1.608$  and  $4.214$  [blue, green and red curves in Fig. 4] respectively. Since these relaxation processes are related to energy exchange between NMs, we expect to see a quantitative difference on how the transitions  $\eta(t=0) = 1 \rightarrow \langle \eta \rangle_G$  are carried.

For the case with  $(\mathcal{H} = 0.307, \Gamma = -0.8)$  [blue curves in Fig. 4(a)], the relaxation of  $\eta(t)$  takes longer, with a timid decrease observed after the curve leaves the unity in the time interval from  $\approx 10^5$  up to around a few  $10^7$  units, which roughly corresponds to the interval on which

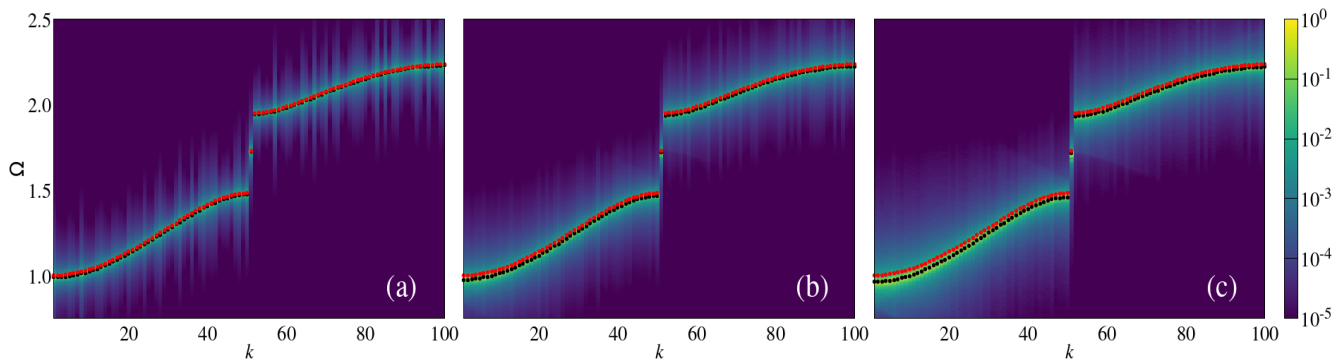


Figure 6.  $\Omega - k$  dependence of the frequency shift distribution  $\langle |a_k(\Omega)|^2 \rangle$  for (a) ( $\mathcal{H} = 2.417, \Gamma = -0.8$ ), (b) ( $\mathcal{H} = 4.409, \Gamma = -0.8$ ) and (c) ( $\mathcal{H} = 7.019, \Gamma = -0.8$ ). The red dots indicate the dispersion relation for the linearized system; whereas the black dots indicate the renormalized dispersion relation for the nonlinear system (see text for details).

we noticed the resonance of a small number of NMs responsible of the system's thermalization in Fig. 3(a). It is also interesting to relate this observation with the temporal behavior of the system's ftMLE,  $\lambda$  [Eq. (15)]. Indeed, in the time period mentioned above, we see that the computed  $\lambda(t)$  of the system [blue curve in Fig. 4(b)] slightly diverges from the one of regular motion  $\lambda(t) \propto \ln t/t$  [black solid line in Fig. 4(b)], confirming the presence of a weakly chaotic dynamics within the system. As time evolves further away from  $t \approx 10^7$ , a saturation of  $\eta(t)$  to values of the order of the Gibbs average  $\langle \eta \rangle_G$  [Eq. (10)] becomes evident. This saturation of the  $\eta(t)$ , is also consistent with the level off of the  $\lambda(t)$ , which further deviates from the behavior observed for regular motion [ $\lambda(t) \propto \ln t/t$ ], indicating the lattice's full chaoticization, and equipartition.

On the other hand, for the cases with ( $\mathcal{H} = 1.608, \Gamma = -0.8$ ) [green curves in Fig. 4] and ( $\mathcal{H} = 4.214, \Gamma = -0.8$ ) [red curves in Fig. 4], the evolution of  $\eta$  falls down quicker and the  $\lambda(t)$  saturates faster toward larger numerical values than the ( $\mathcal{H} = 0.307, \Gamma = -0.8$ ) case due to the faster energy spreading and stronger chaotic behavior. It is worth mentioning that in the case ( $\mathcal{H} = 4.214, \Gamma = -0.8$ ), we observe the presence of an intermediate plateau in the evolution of  $\eta(t)$  in Fig. 4(a), at  $t \approx 10^3$ , which is associated to the presence in the system of metastable states [50] visible in Fig. 5(a). These transient states are unstable discrete breathers (DBs) originating from the degradation of the initial topological nonlinear edge state, chaotically scattering within the lattice and shedding their energy toward the bulk [Fig. 5(a)]. In Fig. 5(b), we compute the associated evolution of the participation number  $P(t)$  [Eq. (14)] and confirm that the disappearance of DBs coincides with the final saturation of the participation number for  $t \approx 10^4$  time units.

The numerical simulations depicted in this section clearly show the presence of two different routes to thermalization of our topological system, namely, in the weak and strong nonlinear (chaos) regimes. In the weak nonlinear limit, the thermalization of the lattice is due to

the activation of a few modes. This reminds what is expected from near exact resonance of NMs well describes in the framework of wave turbulence theory (see, e.g. [45, 46, 51]). On the other hand, in the strong nonlinear regime, a large number of modes are initially resonating leading to stronger chaotic dynamics and faster thermalization. How this behavior is connected with the strong instability predicted by the linear Floquet stability analysis, and a potential Chirikov resonance-overlap conditions [70, 72], is a subject under current investigation.

## B. Renormalized frequency and resonances broadening

In the following numerical calculations, we perform ensemble average (denoted by  $\langle \cdot \rangle$ ) over 200 to 600 realizations, where different random phases  $\varepsilon_k = \pm 10^{-2}$  are implemented in to [Eq. (17)]. For these sets of initial conditions, we have checked that the computed average rescaled entropy  $\langle \eta(t) \rangle$  matches with a good accuracy the one of thermalized modes in the Gibbs description  $\langle \eta \rangle_G$  [Eq. (10)] and that our average ftMLE,  $\langle \lambda(t) \rangle$  has saturated to a constant positive value. We then follow the same procedure as in Ref. [46] in order to extract the spectral characteristics of our multidimensional nonlinear system [Eq. (1)]. That is to say, after reaching the Gibbs statistical equilibrium of the modal energies, we record the  $a_k(t)$  [Eq. (3)] for a time window of about  $500T_1$  time units, where  $T_1$  is the period of the mode with the smallest  $\omega_k(\gamma)$ . Then for each mode  $k$ , the standard discrete Fourier transform [73] is implemented, switching our independent variable  $t \rightarrow \Omega$ . We generate the ensemble average power spectrum  $\langle |a_k(\Omega)|^2 \rangle$ , which has duly been rescaled by its maximum for each mode  $k$ . Consequently, we derive the model's dispersion relation from our numerical data,

$$\tilde{\omega}_k = \left\{ \Omega / \langle |a_k(\Omega)|^2 \rangle = \max_{\Omega'} \langle |a_k(\Omega')|^2 \rangle \right\}. \quad (18)$$

Note that if the system [Eq. (1)] is linear, i.e.  $\mathcal{H} = \mathcal{H}_2$ , we have  $\langle |a_k(\Omega)|^2 \rangle = \delta_{\Omega, \omega_k}$ , and we get  $\tilde{\omega}_k = \omega_k$  from [Eq. (18)]. The  $\Omega - k$  dependence of  $\langle |a_k(\Omega)|^2 \rangle$  is plotted for ( $\mathcal{H} = 2.417, \Gamma = -0.8$ ) in Fig. 6(a), for ( $\mathcal{H} = 4.409, \Gamma = -0.8$ ) in Fig. 6(b) and for ( $\mathcal{H} = 7.019, \Gamma = -0.8$ ) in Fig. 6(c). We observe that the calculated dispersion relation [black dots in Fig. 6] shifts away from the dispersion relation of the linearized system [red dots in Fig. 6] toward smaller values of the frequency, while at the same time a broadening of the distribution of frequency shift appears for each wave number. This renormalization of the frequencies i.e.,  $\omega_k \rightarrow \tilde{\omega}_k$ , as well as the broadening of their distributions, becomes stronger, thus more evident for increasing values of  $\mathcal{H}$  [Eq. (1)].

In App. C, we present additional results on the dependence of the renormalized frequency  $\tilde{\omega}_k$  [Eq. (18)], the width of the frequency broadening  $\chi_k$  [Eq. (C1)] and the MLE  $\Lambda$  [Eq. (16)] on the energy (nonlinearity) of the system.

The above observations are in line with the recent works on nonlinear lattice thermalization [14, 17, 45, 46, 51, 52, 74, 75]. In those studies, the broadening of the width of the distribution of frequency shifts is attributed to the presence of the nonlinearity in the system, which introduces a degree of stochasticity (chaoticity) in the modes' interactions [70, 72]. Besides, the nonlinear frequency shift was investigated for finite chain (e.g.  $n = 16, 32, 64$  and 128) of various lattices including the monoatomic  $\alpha$ - and  $\beta$ -FPUT models and the KG systems as well as the diatomic  $\alpha$ -FPUT lattice. In connection to the monoatomic  $\beta$ -FPUT, it was found that the shift in frequency is due to both trivial [52] and nontrivial [74] four-wave resonances, while for the  $\alpha$ -FPUT counterpart, only trivial four-wave resonances are the drivers of this shift [45]. The later type of mode resonance is also relevant for the quartic KG system [17, 49]. Furthermore, in the case of the diatomic  $\alpha$ -FPUT chain, three-wave resonances are responsible for the renormalization of frequencies [75]. As such, it is pertinent to give a closer look toward which resonant processes are involved in the present model of Fig 1, something we plan to tackle in future endeavours.

### C. Symmetry of the renormalized squared dispersion relation

We now look on potential symmetry properties of the numerically computed squared renormalized dispersion relation,  $\tilde{\omega}_k^2$  [Eq. (18)]. As we stressed in Sec. III, an important characteristic of the eigenvalues  $\omega_k^2$  is their symmetry about their mid-gap, a consequence of chiral symmetry of the dynamical matrix in the linear limit i.e.  $\Gamma = 0$  in  $\mathcal{H}$  in Eq. (1) (see also Fig 2). It is therefore relevant to investigate what is the effect of nonlinearity on this symmetry, by checking the renormalized dispersion relation. In Fig. 7, we plot the change in the squared

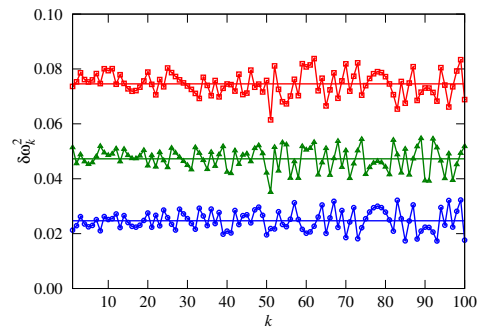


Figure 7. Change in the squared frequency  $\delta\omega_k^2 = \omega_k^2 - \tilde{\omega}_k^2$  [Eq. (19)] of the dispersion relation at different energy levels:  $\mathcal{H} = 2.417$  (blue line-connected circles),  $\mathcal{H} = 4.214$  (green line-connected triangles) and  $\mathcal{H} = 7.019$  (red line-connected squares). For all cases,  $\Gamma = -0.8$ . The horizontal solid lines of the same colors indicate the average values  $\overline{\delta\omega^2}$  of the relevant data points they fit:  $\overline{\delta\omega^2} \approx 0.025 \pm 0.004, 0.047 \pm 0.004$  and  $0.074 \pm 0.004$ , respectively for the blue, green and red line-connected points.

frequency

$$\delta\omega_k^2 = \omega_k^2 - \tilde{\omega}_k^2 = (1 - \eta_k^2) \omega_k^2, \quad \eta_k = \frac{\tilde{\omega}_k}{\omega_k}, \quad (19)$$

for each wave number,  $k$  using three set of parameters ( $\mathcal{H} = 2.417, \Gamma = -0.8$ ) (blue circles), ( $\mathcal{H} = 2.417, \Gamma = -0.8$ ) (green triangles) and ( $\mathcal{H} = 7.019, \Gamma = -0.8$ ) (red squares). In Eq. (19)  $\eta_k$  is the renormalization factor of the frequency of mode  $k$  [74]. Note that  $\eta_k = 1$  in the linear limit, while being  $\eta_k < 1$  for  $\tilde{\omega}_k < \omega_k$  [see e.g., Figs. 12(a), (c) and (e) in App. C] in case  $\Gamma < 0$  [46]. On the other hand, if  $\delta\omega_k^2$  remains practically constant for all values of  $k$ , we can conclude that the squared renormalized dispersion relation is uniformly shifting away from the linear one, keeping thus its subsequent symmetry around the renormalized, squared mid gap frequency  $\tilde{\omega}_{k=51}^2$ . Remarkably, in Fig. 7, we see that this is the case for all the studied energy values. We note that increasing the value of  $\mathcal{H}$  results in higher  $\overline{\delta\omega_k^2}$  values which are fluctuating around the averages  $\overline{\delta\omega^2} \approx 0.025, 0.047$  and  $0.074$ , blue, green and red horizontal lines, for respectively  $\mathcal{H} = 2.417, 4.214$  and  $7.019$ . Hence, we deduce that the contribution of the nonlinear part of the system renormalizes the squared dispersion relation  $\omega_k^2$  in a way that it retains the symmetry inherited from chiral symmetry of the dynamical matrix of the linearized model.

### D. Neighborhood of stable nonlinear topological edge states

Up to now, we have considered the cases of linearly unstable topological edge states. One of the remarkable results of Ref. [32], is the existence of linearly stable topological edge states under strong nonlinearity. Here,



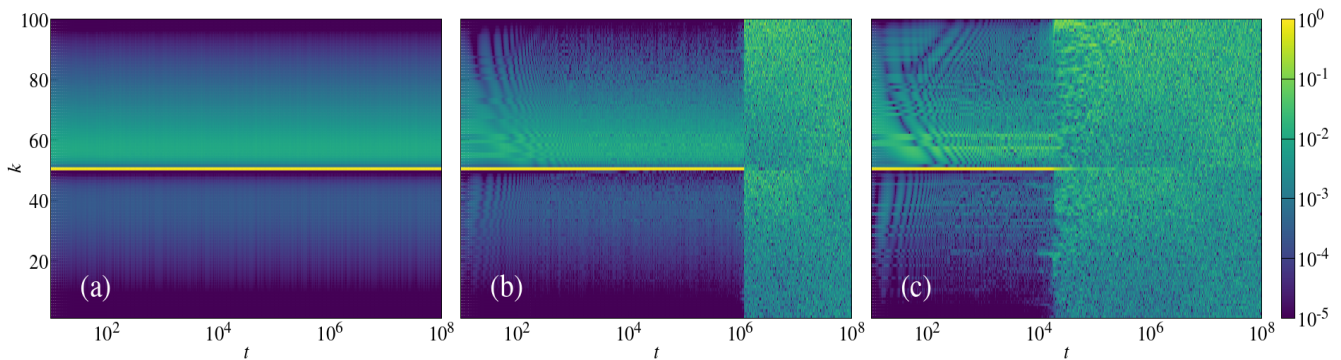


Figure 8. Similar to Fig. 3 but for three different perturbation strengths  $\varepsilon$  [Eq. (17)] of the nonlinear topological edge state at ( $\mathcal{H}=3.779, \Gamma=0.8$ ) with (a)  $\varepsilon = 0.01$ , (b)  $\varepsilon = 0.25$  and (c)  $\varepsilon = 1.0$ , see text for details. Each mode's number is colored according to the intensity of its energy.

we want to understand how robust the stable nonlinear topological edge states are under the system's perturbation. We consider the nonlinear topological edge state at ( $\mathcal{H} = 3.779, \Gamma = 0.8$ ) [shown in Fig.2(c)] applying random perturbations of the form  $\varepsilon_k = \pm\varepsilon$  with  $\varepsilon > 0$  referred to as perturbation parameter, see Fig. 8. The amplitude profiles of  $\nu_k(t)$  corresponding to representative realizations of three different perturbation parameters [see Eq. (17)] with  $\varepsilon = 0.01$ , Fig. 8(a),  $\varepsilon = 0.25$ , Fig. 8(b) and  $\varepsilon = 1$  in Fig. 8(c) are plotted. For the smallest perturbation parameter [Fig. 8(a)], the initially excited modes  $a_k^b(t=0)$  retain their energy  $E_k = \omega_k |a_k(t=0)|^2$  and the lattice remains unthermalized up to the largest simulation time  $t = 10^8$ . Thus, in this case, the nonlinear topological state appears to be stable under the added perturbations. As the magnitude of the perturbation parameter  $\varepsilon \rightarrow \mathcal{O}(1)$  [Figs. 8(c) and (d)], we see that the obtained initial states eventually lead to equipartition in the lattice after time scales that vary with  $\varepsilon$  [Eq. (17)]. This hints us on the fact that there exists a limiting value of the perturbation  $\varepsilon_c$  above which the coherence of the stable nonlinear topological edge state is lost.

In general, the stability properties of autonomous Hamiltonian system's are well described in the framework of phase space dynamics. Indeed, we expect stable nonlinear topological edge states to belong to regular 'islands' surrounded by chaotic 'sea' [71, 76]. In the prospective of Secs. VA and VB, a system's orbit belonging to a regular island does not lead to the system's thermalization in real (NM) space, while the one within the chaotic sea does. If we further assume that the stable topological edge state lies at the center of the island of stability, we define the distance

$$d = \|\mathbf{X}_\varepsilon(0) - \mathbf{X}^b(0)\|, \quad (20)$$

which tells us how far we are from the topological edge state, i.e., the radius of the regular island [76]. In Eq. (20),  $\mathbf{X}^b$  is the topological edge state obtained from the procedure explained in Sec. III and  $\mathbf{X}_\varepsilon$  its perturbed state [which depends on  $\varepsilon$  of Eq. (17)], while  $\|\cdot\|$  stands

again for the Euclidean norm. In order to obtain a reliable measurement of the phase space observable  $d$  [Eq. (20)], the phase space landscape has to remain unchanged as we perturb  $\mathbf{X}^b$ . Consequently, after applying Eq. (17), we particularly take care that the final initial condition  $\mathbf{X}_\varepsilon(0)$  possesses the same energy as  $\mathbf{X}^b$  up to the 10th digit via a Newton-Raphson procedure [73]. The numerically computed values of  $d$  show that it grows exponentially with increasing  $\varepsilon$  values [see inset of Fig. 9].

For a specific perturbation strength  $\varepsilon$ , the choice of different sets of phases  $\varepsilon_k = \pm\varepsilon$ , gives initial conditions of distance  $d$  from the topological edge state in the phase space. We categorize each of these initial conditions as leading or not to thermalization by computing the rescaled spectral entropy  $\eta(t)$  [Eq. (7)]. Then, based on observations of our numerical simulations like that of thermalized states which have  $\eta(t) \approx \langle \eta \rangle_G$ , we introduce the threshold

$$\eta_{th} = 0.2, \quad (21)$$

such that trajectories with  $\eta(t = 10^8) \leq \eta_{th}$  are considered to lead to the lattice thermal equilibrium. In this way, we can define the fraction [16, 77]

$$f_{th} = \frac{R_{th}}{R}, \quad (22)$$

of orbits conducting to the lattice's thermalization. Here,  $R_{th}$  is the number of orbits leading to energy equipartition and  $100 \leq R \leq 300$  is the total number of initial conditions of distance  $d$  from the topological edge state  $\mathbf{X}^b(t=0)$ .

To explore the neighborhood of the linearly stable, nonlinear, topological edge states, we calculate the fraction of thermalized states,  $f_{th}$  [Eq. (22)] at different distances,  $d$  [Eq. (20)] from the topological, nonlinear edge state in the phase space for the parameters ( $\mathcal{H} = 3.779, \Gamma = 0.8$ ) and ( $\mathcal{H} = 8.367, \Gamma = 0.8$ ), Fig. 9. We see that for  $d \rightarrow 0$  all the system orbits are regular i.e.,  $f_{th} \rightarrow 0$ . On the other hand, for  $d \rightarrow \mathcal{O}(1)$ , all the orbits lead to the system thermalization as  $f_{th} \rightarrow 1$ .

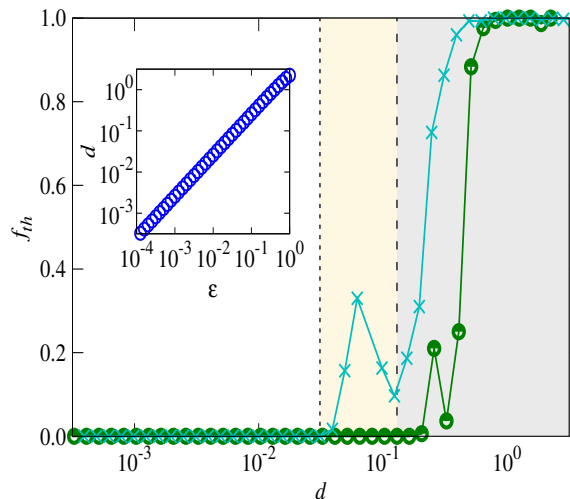


Figure 9. Fraction of thermalized  $f_{th}$  [Eq. (22)] states of the system [Eq. (1)] at time  $t = 10^8$  as function of the distance  $d$  [Eq. (20)] from the linearly stable nonlinear topological state in the phase space with  $(\mathcal{H} = 3.779, \Gamma = 0.8)$  [green line-connected circles] and  $(\mathcal{H} = 8.367, \Gamma = 0.8)$  [cyan line-connected crosses]. The inset panel shows the dependence of  $d$  against the perturbation parameter  $\varepsilon$  of Eq. (17). The dashed vertical line indicates  $d_c \approx 0.13$  and the dotted one  $d_c \approx 0.031$  (see text for details).

For intermediate values of  $d$ , the transition of  $f_{th} = 0 \rightarrow 1$  takes place for all nonlinear strengths. The critical distance  $d_c$  above which  $f_{th} > 0$  represents a length scale above which the system is likely to thermalize and the topological edge state to lose its robustness to the perturbation. Interestingly enough, we observe that  $d_c$  decrease with increasing energy as  $d_c \approx 0.13$  [dashed vertical line in Fig. 9] for the case with the smallest energy  $(\mathcal{H} = 3.779, \Gamma = 0.8)$ , dotted curves of Fig. 9 and  $d_c \approx 0.031$  [dotted dotted line in Fig. 9] for the case with the largest energy  $(\mathcal{H} = 8.367, \Gamma = 0.8)$ , crossed curves of Fig. 9. Once again, this observation is in agreement with the fact that islands of stability tend to disappear for large energy (nonlinearity) values in conservative Hamiltonian models [78].

Eventually when a stable topological edge state destabilizes due to the addition of perturbations, another related question is to know whether the resulting thermalized lattice state possesses similar spectral properties as for the unstable topological edge states seen in Secs. VA and VB. The noticeable difference between stable and unstable nonlinear topological edge states leans on the fact that their existence depends on the type of nonlinearity within the lattice model [32]. Therefore, stable topological edge states are observed for stiffening nonlinear coefficients, i.e.  $\Gamma > 0$  in  $\mathcal{H}$  [Eq. (1)], while unstable topological edge states are mostly associated with softening nonlinear strengths, i.e.  $\Gamma < 0$  in  $\mathcal{H}$  [Eq. (1)].

We numerically investigate the thermalization of the lattice [Eq. (1)], when initially small random phases  $\varepsilon_k =$

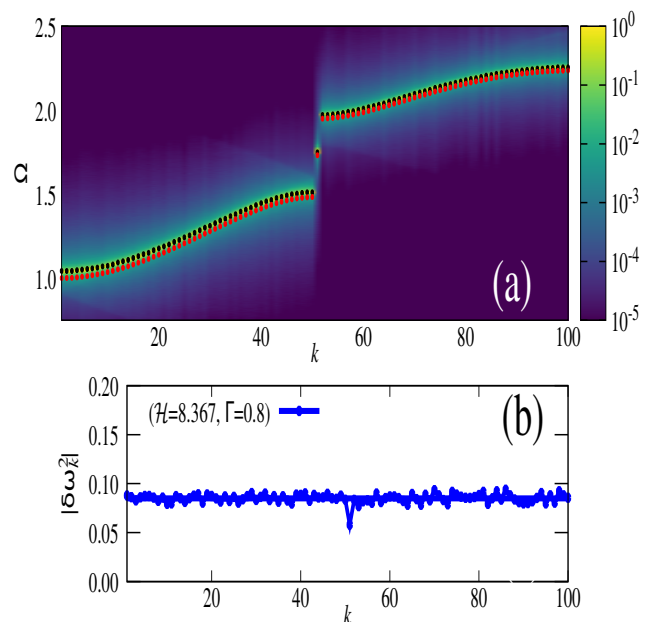


Figure 10. (a) Similar to Fig. 6 but for a perturbation of the stable topological state with  $(\mathcal{H} = 8.367, \Gamma = 0.8)$  at distance  $d \approx 0.285$  (see text for details). The red dotted line represents the dispersion relation of the linearized system  $\omega_k$ , while the black dotted line is the calculated dispersion relation  $\tilde{\omega}_k$  [Eq. (18)]. (b) Change in the squared frequency  $|\delta\omega_k^2|$  [Eq. (19)] (blue line-connected points) of the dispersion relations in panel (a). The value of  $|\delta\omega_k^2|$  is oscillating around the average  $\overline{\delta\omega^2} = 0.085 \pm 0.005$  [blue bold line in (b)].

$\pm 10^{-2}$  [Eq. (17)] are added to the modes of an unstable perturbation at distance  $d \approx 0.285$  of the stable topological edge state with parameter  $(\mathcal{H} = 8.367, \Gamma = 0.8)$ . We then follow the same procedure describe in Sec. VB in order to extract the spectral properties of the system at thermal equilibrium. In Fig. 10(a), we plot the density spectrum  $\langle |a_k(\Omega)|^2 \rangle$  in the  $\Omega - k$  space and extract the system's dispersion relation  $\tilde{\omega}_k$  [Eq. (18)]. These results show that the henceforth calculated dispersion relation  $\tilde{\omega}_k$  [black points in Fig. 10(a)] is shifted upward compared to the one of the linearized model  $\omega_k$  [red points in Fig. 10(a)]. On the other hand, each mode,  $k$ , is characterized by a distribution of frequencies as seen in Sec. VB, which makes it possible, also, in the stiffening case ( $\Gamma > 0$ ) for wave-wave interactions. In addition, we plot in Fig. 10(b) the change in the squared frequencies  $|\delta\omega_k^2|$  [Eq. (19)]. We find that, for increasing value of the wave number,  $k$ , the  $|\delta\omega_k^2|$  remains practically constant, oscillating around the average value  $\overline{\delta\omega^2} \approx 0.085$ . For this reason, we also conclude that the lattice's thermal equilibrium in the case of stiffening nonlinearity is characterized by a renormalized dispersion relation which preserves the chiral symmetry of the underpinning system's dynamical matrix.

## VI. CONCLUSION

We conducted a detailed numerical study of the energy spreading in a nonlinear topological lattice. In particular, we focused on the long-time dynamics of the nonlinear edge states, which are obtained by nonlinear continuation of the edge states of the linearized lattice. Linearly *unstable* edge states were shown to be delocalized from the edges in Ref. [32]. Here we showed that such delocalization is followed by chaos and leads to the thermalization of the lattice. The time to thermalization reduced with the increase of the nonlinear edge state's energy. We also observed an effective renormalization of the dispersion relation of the linearized model, and a broadening of the distribution of the renormalized frequencies for all modes within the lattice.

We also investigated the robustness of the linearly *stable* nonlinear topological states by adding random perturbations to the initial state, and thus moving away from its trajectory in the phase space. Our results showed that these nonlinear edge states remain robust up until a threshold of perturbation, beyond which we witness the loss of robustness because the related trajectory entering into a chaotic region of the phase space. Also, this threshold decreases upon increasing the energy of the system. We also observed an effective renormalization of the dispersion relation similar to the case above.

Finally, we discovered that the effective renormalization of the dispersion relation retains a unique symmetry, i.e., its square is symmetric about the squared mid-band frequency, reminiscent of chiral symmetry in the linearized system. This indicates that the classical symmetries of linear topological lattices in general could have their signature in the renormalized dispersion relation of their nonlinear counterparts.

We believe that this work provides an interesting outlook into the thermalization of topological lattice systems and especially starting with initial conditions in the neighborhood of unstable nonlinear edge states. These states are (unstable) quasi-periodic orbits in the phase space, whose evolutions usually transit smoothly from regular to chaotic behaviors, therefore providing us with the opportunity to better understand the causes of energy spreading in nonlinear discrete lattices. Nonetheless, these results raised a number of significant questions worth investigating in the future. More specifically, how the Floquet stability of the topological edge mode [32] connects to the mode's resonance theory (e.g., discrete mode resonances [45], Chirikov resonance-overlap [72]) of thermalization of discrete lattice model? As such, expressing the mode resonance conditions of the present system along the directions of [45, 46, 51, 75] is relevant for this problem. Additionally, understanding how the above mechanisms change with the type of initial conditions and/or the nonlinearity of the system is also an interesting line in order to construct a more general framework of thermalization on topological lattice systems. Such work could give us a ground to better un-

derstand the transport of energy in nonlinear topological systems and comparing them with those of generic lattice models (see e.g. [9]). Thus, appreciate the influence of topologically protected nonlinear modes on the long time dynamics of topological systems. At last, extending this work to lattices with higher spatial dimensions is also a natural extension of the present study.

## ACKNOWLEDGMENTS

The authors would like to thank the Centre for High Performance Computing (CHPC) of South Africa [79] as well as the High Performance Computing facility of the University of Cape Town [80] for providing their computational resources.

### Appendix A: Symplectic integration of the equations of motion and variational equations of the Su-Schrieffer-Heeger type Klein-Gordon lattice model

In this section we present how we integrate the equations of motion and the variational equations of the Su-Schrieffer-Heeger type Klein-Gordon lattice model [Eq. (1)] using a symplectic integration scheme along with the *tangent map method* [64, 81, 82]. The Hamiltonian  $\mathcal{H}$  [Eq. (1)] can be separated into two integrable parts, namely

$$\mathcal{H} = \mathcal{A}(\mathbf{p}) + \mathcal{B}(\mathbf{x}), \quad (\text{A1})$$

where  $\mathbf{x} = (x_1, x_2, \dots, x_n)$  and  $\mathbf{p} = (p_1, p_2, \dots, p_n)$  are respectively the system's conjugate position and momentum vectors in the phase space, which is characterized by a vector  $\mathbf{X}(t) = (\mathbf{x}(t), \mathbf{p}(t))$ . In this context, we have

$$\mathcal{A}(\mathbf{p}) = \frac{1}{2} \sum_{j=1}^n p_j^2, \quad (\text{A2})$$

and

$$\begin{aligned} \mathcal{B}(\mathbf{x}) = & \sum_{j=1}^n \left[ \frac{\gamma_0}{2} x_j^2 + \frac{\Gamma}{4} x_j^4 \right] \\ & + \frac{1}{4} \sum_{\substack{j=1 \\ j=\text{odd}}}^n \left[ (1 + \gamma) (x_j - x_{j-1})^2 + (1 - \gamma) (x_{j+1} - x_j)^2 \right] \\ & + \frac{1}{4} \sum_{\substack{j=0 \\ j=\text{even}}}^n \left[ (1 - \gamma) (x_j - x_{j-1})^2 + (1 + \gamma) (x_{j+1} - x_j)^2 \right] \end{aligned} \quad (\text{A3})$$

where  $n$  is the number of nonlinear oscillators. Note that in both  $\mathcal{A}$  [Eq. (A2)] and  $\mathcal{B}$  [Eq. (A3)] fixed and free boundary conditions are respectively applied at the left ( $j = 0$ ) and right ( $j = n + 1$ ) edges of the lattice.

In the Lie formalism, the Hamilton equations of motion governing the evolution of an orbit starting at  $\mathbf{X}(0)$ , along with its variational equations, which govern the evolution of a small perturbation  $\mathbf{W}(0) = \delta\mathbf{X}(0)$  from this orbit [64, 83, 84] are

$$\dot{\mathbf{Z}} = \mathbf{L}_{\mathcal{H}\mathcal{V}}\mathbf{Z} = (\mathbf{L}_{\mathcal{A}\mathcal{V}} + \mathbf{L}_{\mathcal{B}\mathcal{V}})\mathbf{Z}, \quad (\text{A4})$$

where  $\mathbf{Z} = (\mathbf{X}, \delta\mathbf{X})$ ,  $(\cdot)$  denotes the time derivative and  $\mathbf{L}_{\mathcal{H}\mathcal{V}}$  is a Lie operator whose general expression can, for example, be found in [64, 84]. Therefore, the solution of the system's dynamical equations [Eq. (A4)] reads

$$\mathbf{Z}(\tau) = e^{\tau(\mathbf{L}_{\mathcal{A}\mathcal{V}} + \mathbf{L}_{\mathcal{B}\mathcal{V}})}\mathbf{Z}(0). \quad (\text{A5})$$

A symplectic integrator consists of approximating the action of the Lie operator  $e^{\tau(\mathbf{L}_{\mathcal{A}\mathcal{V}} + \mathbf{L}_{\mathcal{B}\mathcal{V}})}$  by a product of subsequent actions of operators  $e^{a_i\tau\mathbf{L}_{\mathcal{A}\mathcal{V}}}$  and  $e^{b_i\tau\mathbf{L}_{\mathcal{B}\mathcal{V}}}$  for appropriately chosen sets of real coefficients  $a_i, b_i$  to achieve a certain accuracy [85, 86]. The later Lie operators can be analytically found to be

$$e^{\tau\mathbf{L}_{\mathcal{A}\mathcal{V}}} := \begin{cases} x'_j = x_j + \tau p_j \\ p'_j = p_j \\ \delta x'_j = \delta x_j + \tau \delta p_j \\ \delta p'_j = \delta p_j \end{cases}, \quad \text{for } 1 \leq j \leq n \quad (\text{A6})$$

and

$$e^{\tau\mathbf{L}_{\mathcal{B}\mathcal{V}}} := \begin{cases} x'_j = x_j & \text{for } 1 \leq j \leq n \\ p'_1 = p_1 + \tau [-\gamma_0 x_1 - \Gamma x_1^3 - (1 + \gamma)x_1 + (1 - \gamma)(x_2 - x_1)] & \\ p'_j = p_j + \tau [-\gamma_0 x_j - \Gamma x_j^3 - (1 + \gamma)(x_j - x_{j-1}) + (1 - \gamma)(x_{j+1} - x_j)] & \text{if } j \text{ odd, } 2 \leq j \leq n - 1 \\ p'_j = p_j + \tau [-\gamma_0 x_j - \Gamma x_j^3 - (1 - \gamma)(x_j - x_{j-1}) + (1 + \gamma)(x_{j+1} - x_j)] & \text{if } j \text{ even, } 2 \leq j \leq n - 1 \\ p'_n = p_n + \tau [-\gamma_0 x_n - \Gamma x_n^3 - (1 + \gamma)(x_n - x_{n-1})] & \text{if } n \text{ odd} \\ p'_n = p_n + \tau [-\gamma_0 x_n - \Gamma x_n^3 - (1 - \gamma)(x_n - x_{n-1})] & \text{if } n \text{ even} \\ \delta x'_j = \delta x_j & \text{for } 1 \leq j \leq n \\ \delta p'_1 = \delta p_1 + \tau [\sigma_1 \delta x_1 + \sigma_2 \delta x_2] & \\ \delta p'_j = \delta p_j + \tau [\sigma_{j-1} \delta x_{j-1} + \sigma_j \delta x_j + \sigma_{j+1} \delta x_{j+1}] & \text{if } j \text{ odd, } 2 \leq j \leq n - 1 \\ \delta p'_j = \delta p_j + \tau [\beta_{j-1} \delta x_{j-1} + \beta_j \delta x_j + \beta_{j+1} \delta x_{j+1}] & \text{if } j \text{ even, } 2 \leq j \leq n - 1 \\ \delta p'_n = \delta p_n + \tau [\sigma_{n-1} \delta x_{n-1} + \sigma_n \delta x_n] & \text{if } n \text{ odd} \\ \delta p'_n = \delta p_n + \tau [\beta_{n-1} \delta x_{n-1} + \beta_n \delta x_n] & \text{if } n \text{ even} \end{cases} \quad (\text{A7})$$

where  $\sigma_1 = -\gamma_0 - 3\Gamma x_1^2 - 2$ ,  $\sigma_2 = 1 - \gamma$ ,  $\sigma_{j-1} = 1 + \gamma$ ,  $\sigma_{j+1} = 1 - \gamma$ ,  $\sigma_j = -\gamma_0 - 3\Gamma x_j^2 - 2$ ,  $\sigma_{n-1} = 1 + \gamma$ ,  $\sigma_n = -\gamma_0 - 3\Gamma x_n^2 - (1 + \gamma)$ , and  $\beta_{j-1} = 1 - \gamma$ ,  $\beta_{j+1} = 1 + \gamma$ ,  $\beta_j = -\gamma_0 - 3\Gamma x_j^2 - 2$ ,  $\beta_{n-1} = 1 - \gamma$ ,  $\beta_n = -\gamma_0 - 3\Gamma x_n^2 - (1 - \gamma)$ .

We implemented in this work the so-called  $\mathcal{AB}_4\mathcal{A}864$  symplectic scheme of order 4 [87, 88] which has proved to be a very efficient integration scheme for 1D lattice Hamiltonian systems [83, 84].

## Appendix B: The connection between the Floquet analysis and the resonant modes in the weak nonlinear limit

We identify the frequencies of the most unstable eigenvectors  $v_i$  associated with the Floquet multipliers (FMs)  $\lambda_i$  which diverge the farthest from the unit circle and map these frequencies to the first resonant modes responsible of the lattice thermalization in the weak nonlinear regime. In practice, the linear stability of a periodic orbit  $\mathbf{X}(0)$  with period  $T$  is estimated by following the time evolution of a small perturbation  $\mathbf{W}(0)$  to  $\mathbf{X}(0)$  (see also Sec. IV B). The temporal evolution of such perturbation

can be expressed as

$$\mathbf{W}(t) = \mathbf{A}(t) \cdot \mathbf{W}(0), \quad (\text{B1})$$

where  $\mathbf{W}(t)$  is the perturbation at time  $t > 0$  and  $\mathbf{A}(t)$  is the *fundamental matrix* of the system's variational equations (see e.g. [32, App. B] and [89] for further details). It follows that the values of the perturbation after a time period  $t = T$  is

$$\mathbf{W}(T) = \mathbf{M} \cdot \mathbf{W}(0), \quad \mathbf{M} = \mathbf{A}(T), \quad (\text{B2})$$

in which  $\mathbf{M}$  is called *monodromy matrix*. Consequently, the stability properties of the periodic orbit  $\mathbf{X}(0)$  are encompassed within the eigen-characteristics of  $\mathbf{M}$  (see e.g. [89–91]). The  $2n$  eigenvalues of  $\mathbf{M}$  are referred to as FMs,  $\lambda_i$  and are associated with  $2n$  eigenvector  $v_i$ . Whether any of the  $|\lambda_i| \neq 1$  (diverges from the unit circle in the complex plane), the periodic orbit  $\mathbf{X}(0)$  is said to be unstable.

In Fig. 11(a), we show the  $\lambda_i$  for the edge breather mode with parameter ( $\mathcal{H} = 0.307, \Gamma = -0.8$ ) and observe the presence 4 FMs (blue dots highlighted inside the box) that lead to the first two most dominant instabilities. These instabilities (in blue) result from the



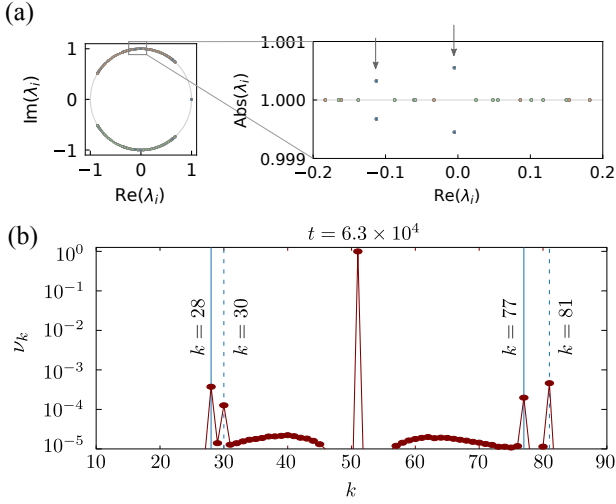


Figure 11. (a) Geometric representation of the FMs  $\lambda_i$  (see text for details) in the complex plane for the topological edge state with parameter ( $\mathcal{H} = 0.307, \Gamma = -0.8$ ) of Fig. 3(a). We superimpose the unit circle to guide the eye. The upper canvas depicts a zoom into the region of the unit circle where the strongest divergence of the FMs from the unit circle takes place. The most unstable eigenvalues are denoted by arrows. (b) Normalized modal energy  $\nu_k(t)$  [Eq. (6)] profile at time  $t \simeq 6.3 \times 10^4$  time units for a representative realization of perturbation of the edge breather mode at ( $\mathcal{H} = 0.307, \Gamma = -0.8$ ). This figure corresponds to a vertical cross section of  $\nu_k(t)$  at ( $t \approx 6.3 \times 10^4, k$ ), see white vertical line of Fig. 3(a). The vertical bold and dotted lines label the resonant modes.

collision of two eigenvalues with opposite Krein signature denoted by orange and green colors. Next, we can co-relate these colliding eigenvalues to the eigenvalues of the linear dispersion band (details can be found in [32, App. B]). We find that the appearance of instability originates from the collisions between the modes  $k = 28$  [resp.  $k = 30$ ] and  $k = 81$  [resp.  $k = 77$ ] of the acoustic and optical bands.

Figure 11(b) show the normalized energy per mode  $\nu_k$  [Eq. (6)] at time  $t \simeq 6.3 \times 10^4$  for a representative simulation using as initial condition the perturbation of the topological edge state with ( $\mathcal{H} = 0.307, \Gamma = -0.8$ ) of Figs. 3(a) and 11. We clearly see that the first 4 resonant modes correspond to the frequencies of the most unstable eigenvectors  $\mathbf{v}_i$  of the Floquet analysis.

### Appendix C: Width $\chi_k$ and frequency shift as a function of energy

To examine the role of the system's nonlinearity we quantify the width  $\chi_k$  of the frequency shift distribution [46]

$$\chi_k = \sqrt{\sum_{\Omega} (\Omega - \tilde{\omega}_k)^2 A_{\Omega,k}}, \quad A_{\Omega,k} = \frac{\langle |a_k(\Omega)|^2 \rangle}{\sum_{\Omega} \langle |a_k(\Omega)|^2 \rangle}, \quad (\text{C1})$$

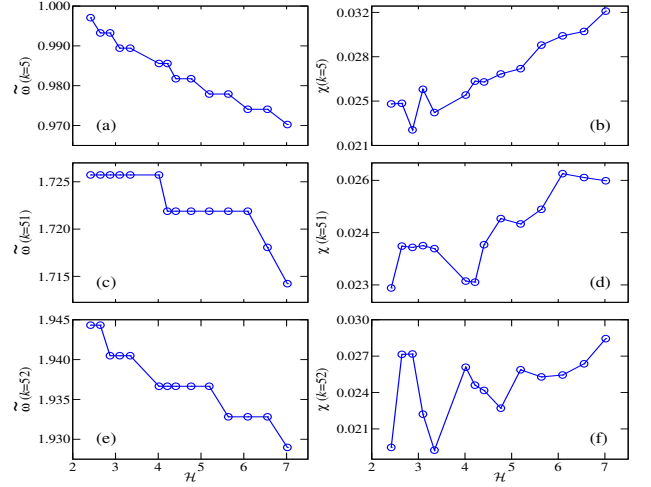


Figure 12. Frequency shift,  $\tilde{\omega}_k = \tilde{\omega}(k)$  [Eq. (18)] [panels (a), (c), (e)] and width of the frequency shift distribution,  $\chi_k = \chi(k)$  [Eq. (C1)] [panels (b), (d), (f)] as functions of the total energy  $\mathcal{H}$  [Eq. (1)] of the system: (a-b)  $k = 5$ , (c-d)  $k = 51$  and (e-f)  $k = 52$ . The ground spring nonlinear coefficient  $\Gamma$ , is fixed at  $\Gamma = -0.8$ .

where  $\Omega$  and  $\tilde{\omega}_k$  [Eq. (18)] are the frequency and renormalized frequency of the  $k$ th mode. We calculate the frequency shift  $\tilde{\omega}_k$  [Eq. (18)] and the broadening of the frequency shift distribution,  $\chi_k$  [Eq. (C1)] for different values of the energy  $\mathcal{H}$  [Eq. (1)], having as an initial condition always the topological linearly unstable nonlinear mode, as shown in Fig. 12. The results are presented for a mode of the lower part of the spectrum ( $k = 5$ ) in Figs. 12(a), (b), for the mode  $k = 51$  at the center of the frequency band in Figs. 12(c), (d) and for a mode at the upper part of the spectrum of frequencies ( $k = 52$ ) in Figs. 12(e), (f). Upon increasing the value of  $\mathcal{H}$ , the  $\tilde{\omega}_k$  is decreasing and the  $\chi_k$  is, in general, growing for all mode numbers. The latter observable, is positively correlated with the system's MLE,  $\langle \Lambda \rangle$  [Eq. (16)] which is linearly increasing, Fig. 13. The somehow non-smooth nature of the trends of  $\tilde{\omega}_k$  and  $\chi_k$  (Fig. 12) can be attributed to the fact that we are exploring small values of the effective nonlinear parameter  $\sim |\Gamma \mathcal{H}_2(t=0)/n| \lesssim 0.006$  [45, 46, 51] for which mild nonlinear effects are experienced by the system. For instance a small degree of chaos,  $\langle \Lambda \rangle \lesssim 0.004$ , seeing in Fig. 13. Nevertheless, it can be conjectured that as the value of the energy increases, the frequency overlap between modes is becoming wider, leading to more prominent resonances between NMs. This results to a faster decay of the energy of the initially excited modes  $a_k^b(t=0)$ , including the one that corresponds to the edge mode ( $k = 51$ ) in which most of the initial energy is located.

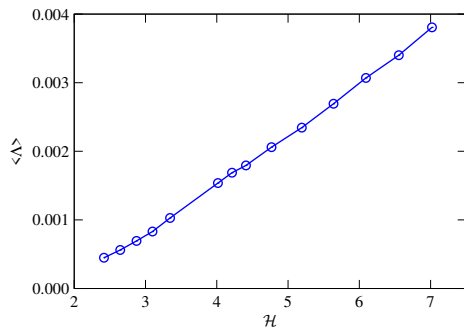


Figure 13. The MLE,  $\langle \Lambda \rangle$  as function of the energy of the system  $\mathcal{H}$  [Eq. (1)]. The value of  $\langle \Lambda \rangle$  grows almost linearly with  $\mathcal{H}$ . We numerically approximated  $\langle \Lambda \rangle$  by  $\langle \lambda(T) \rangle$ , the ftMLE at the end of the integration time  $T$  for each set of parameters in the lattice. The parameters used in  $\mathcal{H}$  [Eq. (1)] are similar to the ones of Fig. 12.

- 
- [1] E. Fermi, P. Pasta, S. Ulam, and M. Tsingou, “Studies of the nonlinear problems,” *Los Alamos Report LA-1940* (1955), 10.2172/4376203.
- [2] J. Ford, “The Fermi-Pasta-Ulam problem: paradox turns discovery,” *Phys. Rep.* **213**, 271–310 (1992).
- [3] G. P. Berman and F. M. Izrailev, “The Fermi–Pasta–Ulam problem: fifty years of progress,” *Chaos* **15**, 015104 (2005).
- [4] D. K. Campbell, P. Rosenau, and G. M. Zaslavsky, “Introduction: the Fermi–Pasta–Ulam problem—the first fifty years,” *Chaos* **15**, 015101 (2005).
- [5] J. De Luca, A. J. Lichtenberg, and M. A. Lieberman, “Time scale to ergodicity in the Fermi–Pasta–Ulam system,” *Chaos* **5**, 283 (1995).
- [6] S. Flach, M. V. Ivanchenko, and O. I. Kanakov, “ $q$ -breathers in Fermi-Pasta-Ulam chains: Existence, localization, and stability,” *Phys. Rev. E* **73**, 036618 (2006).
- [7] A. Ponno, H. Christodoulidi, Ch. Skokos, and S. Flach, “The two-stage dynamics in the Fermi-Pasta-Ulam problem: From regular to diffusive behavior,” *Chaos* **21**, 043127 (2011).
- [8] G. Benettin, H. Christodoulidi, and A. Ponno, “The Fermi-Pasta-Ulam problem and its underlying integrable dynamics,” *J. Stat. Phys.* **152**, 195–212 (2013).
- [9] H. Christodoulidi, T. Bountis, C. Tsallis, and L. Drossos, “Dynamics and statistics of the Fermi–Pasta–Ulam  $\beta$ -model with different ranges of particle interactions,” *Chaos* **26**, 123206 (2016).
- [10] A. Carati, L. Galgani, A. Maiocchi, F. Gangemi, and R. Gangemi, “The FPU problem as a statistical-mechanical counterpart of the KAM problem, and its relevance for the foundations of physics,” *Regul. Chaotic Dyn.* **23**, 704 (2018).
- [11] KØ Rasmussen, T. Cretegny, P. G. Kevrekidis, and N. Grønbech-Jensen, “Statistical mechanics of a discrete nonlinear system,” *Phys. Rev. Lett.* **84**, 3740 (2000).
- [12] B. Rumpf, “Transition behavior of the discrete nonlinear Schrödinger equation,” *Phys. Rev. E* **77**, 036606 (2008).
- [13] S. Iubini and A. Politi, “Chaos and localization in the discrete nonlinear Schrödinger equation,” *Chaos, Solitons & Fractals* **147**, 110954 (2021).
- [14] S. Flach, D. O. Krimer, and Ch. Skokos, “Universal spreading of wave packets in disordered nonlinear systems,” *Phys. Rev. Lett.* **102**, 024101 (2009).
- [15] B. Senyange, B. Many Manda, and Ch. Skokos, “Characteristics of chaos evolution in one-dimensional disordered nonlinear lattices,” *Phys. Rev. E* **98**, 052229 (2018).
- [16] M. Mulansky, K. Ahnert, A. Pikovsky, and D. L. Shepelyansky, “Dynamical thermalization of disordered nonlinear lattices,” *Phys. Rev. E* **80**, 056212 (2009).
- [17] L. Pistone, M. Onorato, and S. Chibbaro, “Thermalization in the discrete nonlinear Klein-Gordon chain in the wave-turbulence framework,” *Euro. Phys. Lett.* **121**, 44003 (2018).
- [18] Ch. Skokos, I. Gkolias, and S. Flach, “Nonequilibrium chaos of disordered nonlinear waves,” *Phys. Rev. Lett.* **111**, 064101 (2013).
- [19] M. Z. Hasan and C. L. Kane, “Colloquium: Topological insulators,” *Rev. Mod. Phys.* **82**, 3045–3067 (2010).
- [20] T. Ozawa, H. M. Price, A. Amo, N. Goldman, M. Hafezi, L. Lu, M. C. Rechtsman, D. Schuster, J. Simon, O. Zeitlinger, and I. Carusotto, “Topological photonics,” *Rev. Mod. Phys.* **91**, 015006 (2019).
- [21] G. Ma, M. Xiao, and C. T. Chan, “Topological phases in acoustic and mechanical systems,” *Nat. Rev. Phys.* **1**, 281 (2019).
- [22] D. Smirnova, D. Leykam, Y. Chong, and Y. Kivshar, “Nonlinear topological photonics,” *Appl. Phys. Rev.* **7**, 021306 (2020).
- [23] B. G.-G. Chen, N. Upadhyaya, and V. Vitelli, “Nonlinear conduction via solitons in a topological mechanical insulator,” *Proc. Natl. Acad. Sci.* **111**, 13004–13009 (2014).
- [24] R. K. Pal, J. Vila, M. Leamy, and M. Ruzzene, “Amplitude-dependent topological edge states in nonlinear phononic lattices,” *Phys. Rev. E* **97**, 032209 (2018).
- [25] R. Chaunsali and G. Theoharis, “Self-induced topological transition in phononic crystals by nonlinearity man-

- agement,” *Phys. Rev. B* **100**, 014302 (2019).
- [26] J. Vila, G. H. Paulino, and M. Ruzzene, “Role of nonlinearities in topological protection: Testing magnetically coupled fidget spinners,” *Phys. Rev. B* **99**, 125116 (2019).
- [27] A. Darabi and M. J. Leamy, “Tunable Nonlinear Topological Insulator for Acoustic Waves,” *Phys. Rev. Applied* **12**, 044030 (2019).
- [28] D. D. J. M. Snee and Y.-P. Ma, “Edge solitons in a nonlinear mechanical topological insulator,” *Extreme Mech. Lett.* **30**, 100487 (2019).
- [29] P.-W. Lo, C. D. Santangelo, B. G.-g. Chen, C.-M. Jian, K. Roychowdhury, and M. J. Lawler, “Topology in nonlinear mechanical systems,” *Phys. Rev. Lett.* **127**, 076802 (2021).
- [30] J. R. Tempelman, K. H. Matlack, and A. F. Vakakis, “Topological protection in a strongly nonlinear interface lattice,” *Phys. Rev. B* **104**, 174306 (2021).
- [31] Y. Lumer, M. C. Rechtsman, Y. Plotnik, and M. Segev, “Instability of bosonic topological edge states in the presence of interactions,” *Phys. Rev. A* **94**, 021801 (2016).
- [32] R. Chaunsali, H. Xu, J. Yang, P. G. Kevrekidis, and G. Theoharis, “Stability of topological edge states under strong nonlinear effects,” *Phys. Rev. B* **103**, 024106 (2021).
- [33] L. Jezequel and P. Delplace, “Nonlinear edge modes from topological 1d lattices,” (2021), [arXiv:2107.10016 \[nlin.PS\]](https://arxiv.org/abs/2107.10016).
- [34] Y.-P. Ma and H. Susanto, “Topological edge solitons and their stability in a nonlinear Su-Schrieffer-Heeger model,” *Phys. Rev. E* **104**, 054206 (2021).
- [35] M. J. Ablowitz, Ch. W. Curtis, and Y.-P. Ma, “Linear and nonlinear traveling edge waves in optical honeycomb lattices,” *Phys. Rev. A* **90**, 023813 (2014).
- [36] Y. Lumer, Y. Plotnik, M. C. Rechtsman, and M. Segev, “Self-localized states in photonic topological insulators,” *Phys. Rev. Lett.* **111**, 243905 (2013).
- [37] Y. Hadad, V. Vitelli, and A. Alu, “Solitons and propagating domain walls in topological resonator arrays,” *ACS Photonics* **4**, 1974 (2017).
- [38] D. Leykam and Y. D. Chong, “Edge solitons in nonlinear-photonic topological insulators,” *Phys. Rev. Lett.* **117**, 143901 (2016).
- [39] A. Bisianov, M. Wimmer, U. Peschel, and O. A. Egorov, “Stability of topologically protected edge states in nonlinear fiber loops,” *Phys. Rev. A* **100**, 063830 (2019).
- [40] K. Mochizuki, N. Kawakami, and H. Obuse, “Stability of topologically protected edge states in nonlinear quantum walks: additional bifurcations unique to Floquet systems,” *J. Phys. A Math. Theor.* **53**, 085702 (2020).
- [41] S. Mukherjee and M. C. Rechtsman, “Observation of Floquet solitons in a topological bandgap,” *Science* **368**, 856–859 (2020).
- [42] S. Mukherjee and M. C. Rechtsman, “Observation of unidirectional soliton-like edge states in nonlinear Floquet topological insulators,” (2020), [arXiv:2010.11359 \[physics.optics\]](https://arxiv.org/abs/2010.11359).
- [43] K. Mochizuki, K. Mizuta, and N. Kawakami, “Fate of topological edge states in disordered periodically driven nonlinear systems,” *Phys. Rev. Res.* **3**, 043112 (2021).
- [44] D. Leykam, E. Smolina, A. Maluckov, S. Flach, and D. A. Smirnova, “Probing band topology using modulational instability,” *Phys. Rev. Lett.* **126**, 073901 (2021).
- [45] M. Onorato, L. Vozella, D. Proment, and Y. V. Lvov, “Route to thermalization in the  $\alpha$ -Fermi-Pasta-Ulam system,” *Proc. Natl. Acad. Sci.* **112**, 4208–4213 (2015).
- [46] Y. V. Lvov and M. Onorato, “Double scaling in the relaxation time in the  $\beta$ -Fermi-Pasta-Ulam-Tsingou model,” *Phys. Rev. Lett.* **120**, 144301 (2018).
- [47] W. P. Su, J. R. Schrieffer, and A. J. Heeger, “Solitons in polyacetylene,” *Phys. Rev. Lett.* **42**, 1698 (1979).
- [48] R. Süsstrunk and S. D. Huber, “Classification of topological phonons in linear mechanical metamaterials,” *Proc. Natl. Acad. Sci.* **113**, E4767–E4775 (2016).
- [49] D. Shirokoff, “Renormalized waves and thermalization of the Klein-Gordon equation,” *Phys. Rev. E* **83**, 046217 (2011).
- [50] C. Danieli, D. K. Campbell, and S. Flach, “Intermittent many-body dynamics at equilibrium,” *Phys. Rev. E* **95**, 060202 (2017).
- [51] L. Pistone, S. Chibbaro, M. Bustamante, Y. V. Lvov, and M. Onorato, “Universal route to thermalization in weakly-nonlinear one-dimensional chains,” *Math. Eng.* **1**, 672 (2019).
- [52] B. Gershgorin, Y. V. Lvov, and D. Cai, “Renormalized waves and discrete breathers in  $\beta$ -Fermi-Pasta-Ulam chains,” *Phys. Rev. Lett.* **95**, 264302 (2005).
- [53] X. Shi, I. Kiropelidis, R. Chaunsali, V. Achilleos, G. Theoharis, and J. Yang, “Disorder-induced topological phase transition in a one-dimensional mechanical system,” *Phys. Rev. Res.* **3**, 033012 (2021).
- [54] S. Flach and A. V. Gorbach, “Discrete breathers — Advances in theory and applications,” *Phys. Rep.* **467**, 1–116 (2008).
- [55] S. Aubry, “Discrete breathers: Localization and transfer of energy in discrete Hamiltonian nonlinear systems,” *Physica D: Nonlin. Phenom.* **216**, 1–30 (2006).
- [56] R. Livi, M. Pettini, S. Ruffo, M. Sparpaglione, and A. Vulpiani, “Equipartition threshold in nonlinear large Hamiltonian systems: The Fermi-Pasta-Ulam model,” *Phys. Rev. A* **31**, 1039 (1985).
- [57] M. Pettini and M. Landolfi, “Relaxation properties and ergodicity breaking in nonlinear Hamiltonian dynamics,” *Phys. Rev. A* **41**, 768 (1990).
- [58] M. Pettini and M. Cerruti-Sola, “Strong stochasticity threshold in nonlinear large Hamiltonian systems: Effect on mixing times,” *Phys. Rev. A* **44**, 975 (1991).
- [59] Ch. G. Goedde, A. J. Lichtenberg, and M. A. Lieberman, “Chaos and the approach to equilibrium in a discrete sine-gordon equation,” *Physica D: Nonlin. Phenom.* **59**, 200–225 (1992).
- [60] G. Benettin, L. Galgani, and J.-M. Strelcyn, “Kolmogorov entropy and numerical experiments,” *Phys. Rev. A* **14**, 2338 (1976).
- [61] G. Benettin, L. Galgani, A. Giorgilli, and J.-M. Strelcyn, “Lyapunov characteristic exponents for smooth dynamical systems and for Hamiltonian systems; a method for computing all of them. Part 1: Theory,” *Meccanica* **15**, 9–20 (1980).
- [62] G. Benettin, L. Galgani, A. Giorgilli, and J.-M. Strelcyn, “Lyapunov characteristic exponents for smooth dynamical systems; a method for computing all of them. Part 2: Numerical application,” *Meccanica* **15**, 21–30 (1980).
- [63] Ch. Skokos, “The Lyapunov characteristic exponents and their computation,” in *Dynamics of Small Solar System Bodies and Exoplanets*, edited by Jean J. Souchay and Rudolf Dvorak (Springer Berlin Heidelberg, Berlin, Heidelberg, 2010) pp. 63–135.

- [64] Ch. Skokos and E. Gerlach, “Numerical integration of variational equations,” *Phys. Rev. E* **82**, 036704 (2010).
- [65] T. Dauxois, S. Ruffo, and A. Torcini, “Modulation estimate for the maximal Lyapunov exponent in Fermi-Pasta-Ulam chains,” *Phys. Rev. E* **56**, R6229 (1997).
- [66] B. Many Manda, B. Senyange, and Ch. Skokos, “Chaotic wave-packet spreading in two-dimensional disordered nonlinear lattices,” *Phys. Rev. E* **101**, 032206 (2020).
- [67] L. Casetti, M. Cerruti-Sola, M. Pettini, and E. G. D. Cohen, “The Fermi-Pasta-Ulam problem revisited: Stochasticity thresholds in nonlinear Hamiltonian systems,” *Phys. Rev. E* **55**, 6566 (1997).
- [68] The localization volume of a normal mode (NM) is the spatial extent on which the mode’s amplitude is not exponentially small. This quantity is often numerically estimated via the participation number of the NM [92]. We compute the localization volume of the linear topological localized edge state in Fig. 2(b) and find its value to be  $\approx 2$ .
- [69] J. L. Marín and S. Aubry, “Finite size effects on instabilities of discrete breathers,” *Physica D: Nonlin. Phenom.* **119**, 163–174 (1998), localization in Nonlinear Lattices.
- [70] F. M. Izrailev and B. V. Chirikov, “The statistical properties of a non-linear string,” (1965).
- [71] C. Antonopoulos and T. Bountis, “Stability of simple periodic orbits and chaos in a Fermi-Pasta-Ulam lattice,” *Phys. Rev. E* **73**, 056206 (2006).
- [72] B. V. Chirikov, “A universal instability of many-dimensional oscillator systems,” *Phys. Rep.* **52**, 263–379 (1979).
- [73] W. H. Press, S. A. Teukolsky, W. T. Vetterling, and B. P. Flannery, *Numerical recipes in Fortran 90 the art of parallel scientific computing* (Cambridge university press, 1996).
- [74] W. J. Shi-xiao, H.-H. Lu, D. Zhou, and D. Cai, “Renormalized dispersion relations of  $\beta$ -Fermi-Pasta-Ulam chains in equilibrium and nonequilibrium states,” *Phys. Rev. E* **90**, 032925 (2014).
- [75] A. Pezzi, G. Deng, Y. Lvov, M. Lorenzo, and M. Onorato, “Three-wave resonant interactions in the diatomic chain with cubic anharmonic potential: theory and simulations,” (2021), [arXiv:2103.08336 \[cond-mat.stat-mech\]](https://arxiv.org/abs/2103.08336).
- [76] T. Bountis, K. Kaloudis, Th. Oikonomou, B. Many Manda, and Ch. Skokos, “Stability properties of 1-dimensional Hamiltonian lattices with nonanalytic potentials,” *Int. J. Bifurc. Chaos* **30**, 2030047 (2020).
- [77] M. Mulansky, “Scaling of chaos in strongly nonlinear lattices,” *Chaos* **24**, 024401 (2014).
- [78] M. Hénon and C. Heiles, “The applicability of the third integral of motion: Some numerical experiments,” *Astron. J.* **69**, 73–79 (1964).
- [79] <https://www.chpc.ac.za/>.
- [80] <http://hpc.uct.ac.za/>.
- [81] E. Gerlach and Ch. Skokos, “Comparing the efficiency of numerical techniques for the integration of variational equations,” *Discr. Cont. Dyn. Sys.-Supp.* **2011**, 475–484 (2011).
- [82] E. Gerlach, S. Eggl, and Ch. Skokos, “Efficient integration of the variational equations of multidimensional Hamiltonian systems: Application to the Fermi–Pasta–Ulam lattice,” *Int. J. Bifurc. Chaos* **22**, 1250216 (2012).
- [83] B. Senyange and Ch. Skokos, “Computational efficiency of symplectic integration schemes: application to multidimensional disordered Klein–Gordon lattices,” *Eur. Phys. J. Spec. Top.* **227**, 625–643 (2018).
- [84] C. Danieli, B. Many Manda, T. Mithun, and Ch. Skokos, “Computational efficiency of numerical integration methods for the tangent dynamics of many-body Hamiltonian systems in one and two spatial dimensions,” *Math. Eng.* **1**, 447–488 (2019).
- [85] H. Yoshida, “Construction of higher order symplectic integrators,” *Phys. Lett. A* **150**, 262–268 (1990).
- [86] E. Hairer, C. Lubich, and G. Wanner, *Geometric numerical integration: structure-preserving algorithms for ordinary differential equations*, Vol. 31 (Springer Science & Business Media, 2006).
- [87] S. Blanes, F. Casas, A. Farres, J. Laskar, J. Makazaga, and A. Murua, “New families of symplectic splitting methods for numerical integration in dynamical astronomy,” *Appl. Num. Math.* **68**, 58–72 (2013).
- [88] A. Farrés, J. Laskar, S. Blanes, F. Casas, J. Makazaga, and A. Murua, “High precision symplectic integrators for the solar system,” *Celest. Mech. Dyn. Astron.* **116**, 141–174 (2013).
- [89] Ch. Skokos, “On the stability of periodic orbits of high dimensional autonomous Hamiltonian systems,” *Physica D: Nonlin. Phenom.* **159**, 155–179 (2001).
- [90] P. G. Kevrekidis, “Instabilities via negative Krein signature in a weakly non-Hamiltonian DNLS model,” *Math. Eng.* **1**, 378–390 (2019).
- [91] M. Chung, Y.-L. Cheon, and H. Qin, “Linear beam stability in periodic focusing systems: Krein signature and band structure,” *Nucl. Instrum. Methods Phys. Res., Sect. A* **962**, 163708 (2020).
- [92] D. O. Krimer and S. Flach, “Statistics of wave interactions in nonlinear disordered systems,” *Phys. Rev. E* **82**, 046221 (2010).